JℲM PAPERS

Damköhler number independent stable regime in reactive radial viscous fingering

Priya Verma[1,2]**, Vandita Sharma**[3,4]**, Ching-Yao Chen**[2],†** and Manoranjan Mishra**[1,5],†

[1]Department of Mathematics, Indian Institute of Technology Ropar, 140001 Rupnagar, Punjab, India

[2]Department of Mechanical Engineering, National Yang Ming Chiao Tung University, 30010 Hsinchu, Taiwan R.O.C.

[3]School of Basic Sciences, Indian Institute of Information Technology Una, 177209, Una, Himachal Pradesh, India

[4]Department of Mathematics and Computing, Dr. B R Ambedkar National Institute of Technology Jalandhar, 144008 Punjab, India

[5]Center of Research for Energy Effeciency and Decarbonization, Indian Institute of Technology Ropar, 140001, Rupnagar, Punjab, India

The impact of a chemical reaction, $A + B \rightarrow C$, on the stability of a miscible radial displacement in a porous medium is established. Our study involves a comprehensive analysis employing both linear stability analysis and nonlinear simulations. Through linear stability analysis, the onset of instability for monotonic as well as non-monotonic viscosity profiles corresponding to the same end-point viscosity are discussed and compared. We establish a (R_b, R_c) phase plane for a wide range of Damköhler number (Da) and Péclet number (Pe) into stable and unstable regions. Here, $R_b = \ln(\mu_B/\mu_A)$ and $R_c = \ln(\mu_C/\mu_A)$ and μ_i is the viscosity of fluid $i \in \{A, B, C\}$. The stable zone in the (R_b, R_c) phase plane contracts with increased Da and Pe but never vanishes. It exists even for $Da \rightarrow \infty$. Interestingly, we obtain a Da independent stable region in the neighbourhood of $R_c = R_b$ where no transition occurs in stability despite changes in reaction rate. The study allows us to acquire knowledge about the transition of the stability for varying Da, Pe and different reactions classified using R_b, R_c.

Key words: fingering instability, Hele-Shaw flows, reacting multiphase flows

1. Introduction

The viscous fingering (VF) instability is a fundamental transport phenomenon manifested by a high mobile fluid penetration in a porous medium saturated with less mobile fluid,

† Email addresses for correspondence: chingyao@nycu.edu.tw, manoranjan.mishra@gmail.com

and this unfavourable viscosity contrast results in the emergence of complex fingering patterns at the fluid–fluid interface. While, for favourable viscosity contrast, the flow remains stable. The VF instability has immense applications ranging from hydrology (Dentz *et al.* 2011), oil recovery (Muggeridge *et al.* 2014; Jiménez-Martínez *et al.* 2016), diagnosis of cancer (Streitberger *et al.* 2020), chromatography separation (Catchpoole *et al.* 2006; Shalliker *et al.* 2007; Rana *et al.* 2019), CO_2 sequestration (Huppert & Neufeld 2014; Chen *et al.* 2017; Babaei & Islam 2018; Fakhari *et al.* 2018), biology (Mainster 1990; Matsushita & Fujikawa 1990; Dong *et al.* 2020; Delannoy *et al.* 2022), polymer flooding (Corredor, Maini & Husein 2018) and lubrication in microfluidics (Cubaud & Mason 2012).

In past decades, several experiments have been conducted to understand the instability. These experiments are performed in the Hele-Shaw cell by injecting less viscous fluid while the cell is filled with a higher viscosity fluid. The Hele-Shaw cell consists of two transparent glass plates separated by a minuscule gap. The flow through it is mathematically analogous to a porous medium (Paterson 1985; Chen 1987). To mimic this instability numerically, we model the miscible flow in porous media by utilizing mass conservation and momentum conservation through the convection–diffusion equation and Darcy's law, respectively. In such flows, the velocity profile plays a pivotal role in determining the stability of the system. Depending on the velocity profile, mainly two types of displacements are studied in the literature: radial and rectilinear in porous media flows. In the rectilinear flow, the interface between fluids remains flat, and fluids displace each other with uniform velocity. In the case of radial flow, the interfacial area increases, and velocity decreases with the radial distance from the source. On account of the spatially dependent velocity profile, the perturbation at the fluid–fluid interface evolves algebraically with time (Tan & Homsy 1987). The algebraic growth of perturbations is significantly slower than the exponential growth of perturbations that takes place in the case of rectilinear flow. It attributes a minimum viscosity ratio between fluids to trigger the instability of radial flow. The transition in the stability of flow has been demonstrated numerically and empirically by Sharma *et al.* (2020). They determine a phase plane between Péclet number and viscosity ratio classified into stable and unstable zones and present the initial radius of the circular region as a control parameter. For decreasing initial radius, the stable region in the phase plane between Péclet number and viscosity ratio is contracted but never vanishes. It persists even when the point source is considered (Tan & Homsy 1987; Bischofberger, Ramachandran & Nagel 2014; Videbæk & Nagel 2019).

A chemical reaction can induce an unfavourable disparity in viscosity, leading to the destabilization of flows within porous media by altering the viscosity distribution and impacting flow stability (Sharma *et al.* 2019). For instance, it is observed that the chemical reaction $A + B \rightarrow C$ can always destabilize the flow more by generating a product having viscosity contrast with the reactants while the viscosity profile depends on reactants and product concentration exponentially (Hejazi *et al.* 2010; De Wit 2020). Such reactive displacements are modelled in several transport phenomena to optimize the efficiency of the process, such as alkaline flooding in enhanced oil recovery processes (Mayer *et al.* 1983), contamination degradation (Richardson & Nicklow 2002), CO_2 sequestration (Liu *et al.* 2011) to cite a few. Depending on the application, chemical reactions in porous media flow may be beneficial. It reduces the interfacial tension and enhances the miscibility that leads to improved mixing and more recovery in transport processes such as chemical flooding in enhanced oil recovery (Mayer *et al.* 1983; Pei *et al.* 2012), frontal polymerization (Pojman 2010) and chemical treatment of oil-bearing formations (De Wit & Homsy 1999). In recent studies, it has been observed that the oil recovery by calcium

hydroxide ($Ca(OH)_2$) flooding is more than that of water flooding for heterogeneous porous media (Mahardika *et al.* 2021). Moreover, the chemical reaction can generate bubbles (Wang *et al.* 2021) that prevent the mixing in porous media (Wang *et al.* 2021). The VF produced by chemical reactions can be employed to improve mixing in a variety of fields at all scales, from macroscales to microscales, and the nonlinear interaction between a chemical reaction and VF instability leads to enhanced mixing between fluids. It has been analysed by several researchers in both ways, experimentally (Nagatsu & Ueda 2001, 2003; Nagatsu *et al.* 2007, 2009; Riolfo *et al.* 2012) and numerically (Gérard & De Wit 2009; Hejazi *et al.* 2010; Sharma *et al.* 2019).

For radial flow, there exists a minimum viscosity contrast to trigger the instability in non-reactive displacements where both the flows are non-reactive in nature (Tan & Homsy 1987; Sharma *et al.* 2020), the same holds for the reactive displacement (Sharma *et al.* 2019). It is reported that when reactants are isoviscous, instability is induced when the product and reactants have sufficient viscosity contrast. This has been observed both through numerical investigations through nonlinear simulations (NLS) (Sharma *et al.* 2019; Verma, Sharma & Mishra 2022) and linear stability analysis (LSA) (Sharma, Chen & Mishra 2023). However, they do not consider the reactive displacements with viscosity mismatched reactants. The critical viscosity contrast reduces when we increase the reaction rate. Further, Kim *et al.* (2021) have performed a LSA for radial flow utilizing spectral analysis restricted to the asymptotic limit of $Dat \rightarrow \infty$, $Pe \rightarrow \infty$. Here Da, Pe and t represent the reaction rate, Péclet number and time, respectively. They obtained critical viscosity ratios that trigger instability and establish a power law trend between Pe and the critical viscosity ratios. Further, they show that the LSA results are supported by NLS. To the best of our knowledge, no theoretical analysis of the radial reactive displacement, when reactants have some viscosity contrast for a finite range of Pe and Da, has been documented in the literature. However, the prevalent focus in most experimental studies is exploring reactive VF caused by reactants with mismatched viscosities (Nagatsu & Ueda 2001; Nagatsu *et al.* 2007, 2009; Riolfo *et al.* 2012). In addition, instabilities often occur even in the absence of a reaction, leading to an analysis of how chemical reactions impact viscous fingering (Hejazi *et al.* 2010; De Wit 2020; Verma, Sharma & Mishra 2023). Moreover, it is observed that when the reactants have an unfavourable viscosity contrast, the reaction can promote or stabilize viscous fingering for rectilinear flow, indicating that the chemical control of local fingering dynamics can be precisely tuned by selecting the appropriate chemical species with a particular difference in concentrations (Hejazi *et al.* 2010; De Wit 2020). However, for radial flow, the literature lacks the numerical investigation of reactive displacement with viscosity mismatched reactants. Thus, it would be intriguing to investigate how the reaction rate influences the transition in stability for radial flow when the reactants have viscosity contrast.

In this study, we fill the above-mentioned literature gap and present a thorough examination that considers the effects of viscosity mismatch between the reactants and product for a range of Da and Pe by performing NLS and LSA. In this work, we introduce an LSA to understand the dynamics of the reactive displacements in transient time. However, we encounter an unsteady base state as a solution of advection–diffusion–reaction equations (Brau, Schuszter & De Wit 2017). The time-dependent nature of this base state renders the stability matrix non-orthogonal. However, it has been observed that if the stability matrix is not orthogonal, the early-time dynamics may not be captured (Trefethen *et al.* 1993; Schmid 2007). Thus, modal analysis is not applied and we opt for non-modal analysis. For optimal initial conditions, we give initial perturbation around the interface instead of the entire r domain, as it is known

as the fastest-growing perturbation (Ben, Demekhin & Chang 2002; Hota, Pramanik & Mishra 2015*b*). Later, we validate all LSA predictions through NLS. Both LSA and NLS predict the critical parameters for instability decay with Péclet number and reaction rate. Our research is novel in the sense that we explore the stability of reactive displacement based on the viscosity profile for radial flow. We determine whether the modifications resulting from a chemical reaction impact the flow stability compared with the equivalent non-reactive situation. We determine a phase plane between the viscosity ratios between the reactants and product, divided by critical viscosity ratios for instability and find that the reactions can affect system stability up to a certain extent. For instance, there exists a stable region in the phase plane for even $Da \to \infty$. Moreover, we report the type of reactive displacement where the stability of the flow is unaffected by Da. For such types of reactions, the product viscosity is the same as the viscosity of the displacing reactant, and it is represented as a Da-independent region in the (R_b, R_c) phase plane.

The organization of the paper is as follows. In § 2 we give the mathematical formulation. We present the base state equations and solve them numerically. Further, we derive the linearized perturbed equations and perform LSA in § 3. Lastly, we perform NLS and compare LSA results with NLS results in § 4 and address the applications of the work in § 5.

2. Mathematical formulation

A miscible displacement is considered in a homogeneous and isotropic porous medium where one fluid, *A*, is injected from the source with flow rate *Q* per unit depth, displacing the other fluid, *B*, radially. Both fluids are Newtonian, neutrally buoyant and reactive. A second-order irreversible chemical reaction

$$A + B \to C, \tag{2.1}$$

occurs in the system whenever both fluids come into contact (figure 1). The system of flow equations consists of the continuity equation and Darcy's law, describing mass conservation and momentum conservation. Further, we couple the flow equations with reaction–convection–diffusion equations that interpret the transport of fluid species. In experiments, the dye concentration is added in displacing fluid initially. The dye is non-reactive in nature with the other fluids and has no impact on the viscosity profile. Further, we consider a convection–diffusion equation describing the transport of dye concentration, *z*. The equations can be represented in non-dimensionalized form as follows (Hejazi *et al.* 2010; Sharma *et al.* 2019):

$$\nabla \cdot \boldsymbol{u} = 0, \tag{2.2a}$$

$$\nabla p = -\mu \boldsymbol{u}, \tag{2.2b}$$

$$\frac{\partial a}{\partial t} + \boldsymbol{u} \cdot \nabla a = \frac{1}{Pe} \nabla^2 a - Da\,ab, \tag{2.2c}$$

$$\frac{\partial b}{\partial t} + \boldsymbol{u} \cdot \nabla b = \frac{1}{Pe} \nabla^2 b - Da\,ab, \tag{2.2d}$$

$$\frac{\partial c}{\partial t} + \boldsymbol{u} \cdot \nabla c = \frac{1}{Pe} \nabla^2 c + Da\,ab, \tag{2.2e}$$

$$\frac{\partial z}{\partial t} + \boldsymbol{u} \cdot \nabla z = \frac{1}{Pe} \nabla^2 z. \tag{2.2f}$$

We employ t_f and $\sqrt{Qt_f}$ as the characteristic scales to non-dimensionalize time and length, respectively, where t_f is the time up to which we inject fluid *A*. Further, we
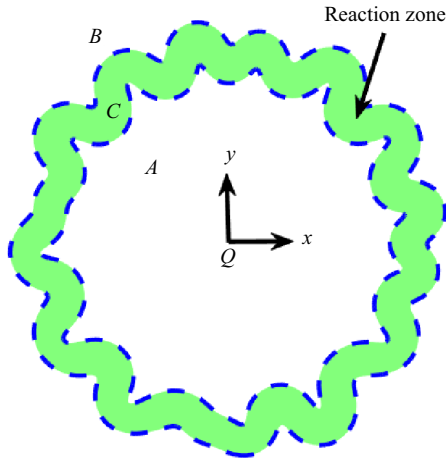
Figure 1. Schematic of the $A + B \rightarrow C$ chemical reaction in a radial source flow. The green-coloured shaded region, bounded by dashed lines, is where both the reactants come into contact and product C is generated. We denote this region as a reaction zone. The outside and inside regions of the reaction zone are occupied by reactants B and A, respectively.

non-dimensionalize Darcy velocity $\boldsymbol{u}$, viscosity μ, pressure p and fluid concentrations (a, b, c) by $\sqrt{Q/t_f}$, μ_A, $Q\mu_A/\kappa$ and a_0, respectively. Here, the concentration and viscosity of reactant A are represented by a_0 and μ_A, respectively, while the porous medium's permeability is represented by κ. It is important to note that t_f represents the duration up to which we want to conduct the study. We discuss the limitations of other choices of length scale in Appendix A. The viscosity profile depends on product and reactant concentrations exponentially as follows (Hejazi *et al.* 2010):

$$\mu = \exp(R_b b + R_c c), \quad R_b = \ln(\mu_B/\mu_A), \quad R_c = \ln(\mu_C/\mu_A). \tag{2.3}$$

We categorize the reactions based on the viscosity of the reactants and product. Every (R_b, R_c) value characterizes the viscosity contrast between B and A; and C and A, respectively. Thus, on changing (R_b, R_c), we change the reactants and product and hence explore a new reaction. The initial conditions associated with (2.2) are

$$(a, b, c, z)(\boldsymbol{x}, t = 0) = \begin{cases} (1, 0, 0, 1), & 0 < |\boldsymbol{x}| < r_0, \\ (0, 1, 0, 0), & \text{otherwise,} \end{cases} \tag{2.4a}$$

$$\boldsymbol{u}(\boldsymbol{x}, t = 0) = \frac{\boldsymbol{x}}{2\pi|\boldsymbol{x}|^2}, \tag{2.4b}$$

where $\boldsymbol{x} = (x, y)$ and r_0 is the initial radius of the circular region filled with fluid A. Here we encounter four non-dimensionalized parameters R_b, R_c, Damköhler number Da and Péclet number Pe. All the fluids are assumed to have the same diffusion coefficient, D, and $Pe = Q/D$, which shows a comparison of fluid transport due to convection and diffusion, while Da is obtained as a ratio of convective time scale and reactive time scale, i.e. $Da = t_f/(1/ka_0)$. Here k is the reaction rate constant.

3. Linear stability analysis

3.1. *Linearized perturbed equations*

In order to carry out a stability analysis, we need to formulate linearized perturbed equations for perturbed fluid concentrations and perturbed velocity around base state flow.
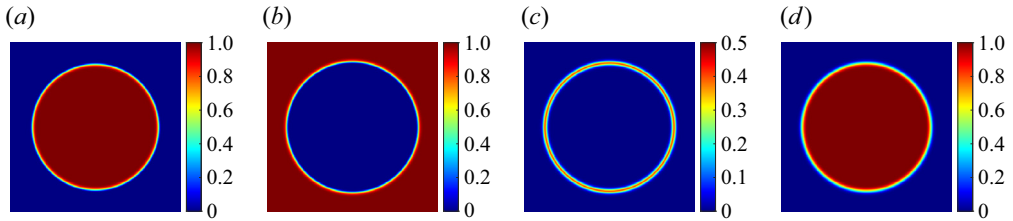
Figure 2. Base state profile of (*a*) reactant *A*, (*b*) reactant *B*, (*c*) product *C* and (*d*) dye concentrations for $Da = 100$, $Pe = 3000$ at final time $t = 1$.

We define (A_0, B_0, C_0, Z_0), base state concentrations of *A*, *B*, *C* and dye as the solution of (2.2*c*)–(2.2*f*) in the absence of any viscosity contrast, i.e. $R_b = R_c = 0$ (Sharma *et al.* 2023). The base state solution is axisymmetric, and it is just a function of radius, *r* only. However, the solutions cannot be attained analytically (Brau *et al.* 2017). Even, for (2.2*f*), provided the initial condition in (2.4), an analytical solution is unattainable (Sharma *et al.* 2020). Thus, we compute the base state concentrations numerically using the method of lines discussed in § 3.2. The density plots of the obtained base state concentrations for $Da = 100$, $Pe = 3000$ are shown in figure 2. For stable displacement, the initial velocity provided by the source does not get perturbed and remains the same as in (2.4*b*). It is considered as the base state velocity, $\boldsymbol{u}_0$. Further, we notice that the base state velocity profile is characterized by a singularity at the origin. To address this singularity, we introduce a Gaussian source of core, σ as proposed by Chen *et al.* (2008) and Sharma *et al.* (2019), resulting in the velocity profile as follows:

$$\boldsymbol{u}_b = \left(x \frac{1 - e^{-(x^2 + y^2)/\sigma^2}}{2\pi(x^2 + y^2)}, y \frac{1 - e^{-(x^2 + y^2)/\sigma^2}}{2\pi(x^2 + y^2)} \right), \quad \sigma \leq r_0. \tag{3.1}$$

Introducing a Gaussian source term can better mimic physical phenomena that smooth out velocity profiles in real-world flows. However, if we were to consider $r_0 \to 0$, we would be unable to utilize this modification due to the constraint $\sigma \leq r_0$. Therefore, we confine our analysis to cases where $r_0 > 0$ and refrain from investigating how the parameter r_0 influences the stability of the reactive flow. Nonetheless, the impact of r_0 on stability has previously been examined in the context of non-reactive flow by Sharma *et al.* (2020). The decrease in r_0 results in reducing the critical viscosity contrast for instability and this r_0 works as a control parameter for instability, which holds for reactive fluids.

After having the base state solution, we perturb the base state profile as follows:

$$(a, b, c, z, \boldsymbol{u}) = (A_0, B_0, C_0, Z_0, \boldsymbol{u}_0) + (a', b', c', z', \boldsymbol{u}'). \tag{3.2}$$

For the ease of the calculations, we redefine the governing equation in stream function–vorticity formulations. We define the stream function as $\psi = \psi_0 + \psi'$, ψ_0 is base state stream function and ψ' is the perturbed component of stream function that is defined as $\boldsymbol{u}' = (-\partial \psi'/\partial y, \partial \psi'/\partial x)$. Thus, the linearized perturbed system of equations

1000 A72-6

can be written in stream function–vorticity formulation as in Sharma *et al.* (2023):

$$\nabla^2 \psi' = -\omega, \qquad (3.3a)$$

$$\omega = R_c(\boldsymbol{u}_0 \times \boldsymbol{\nabla} c' + \boldsymbol{u}' \times \boldsymbol{\nabla} C_0) \cdot \hat{\boldsymbol{k}} + R_b(\boldsymbol{u}_0 \times \boldsymbol{\nabla} b' + \boldsymbol{u}' \times \boldsymbol{\nabla} B_0) \cdot \hat{\boldsymbol{k}}, \qquad (3.3b)$$

$$\frac{\partial a'}{\partial t} + \boldsymbol{u}_0 \cdot \boldsymbol{\nabla} a' + \boldsymbol{u}' \cdot \boldsymbol{\nabla} A_0 = \frac{1}{Pe}\nabla^2 a' - Da(B_0 a' + A_0 b'), \qquad (3.3c)$$

$$\frac{\partial b'}{\partial t} + \boldsymbol{u}_0 \cdot \boldsymbol{\nabla} b' + \boldsymbol{u}' \cdot \boldsymbol{\nabla} B_0 = \frac{1}{Pe}\nabla^2 b' - Da(B_0 a' + A_0 b'), \qquad (3.3d)$$

$$\frac{\partial c'}{\partial t} + \boldsymbol{u}_0 \cdot \boldsymbol{\nabla} c' + \boldsymbol{u}' \cdot \boldsymbol{\nabla} C_0 = \frac{1}{Pe}\nabla^2 c' + Da(B_0 a' + A_0 b'), \qquad (3.3e)$$

$$\frac{\partial z'}{\partial t} + \boldsymbol{u}_0 \cdot \boldsymbol{\nabla} z' + \boldsymbol{u}' \cdot \boldsymbol{\nabla} Z_0 = \frac{1}{Pe}\nabla^2 z'. \qquad (3.3f)$$

Here ω is the $\hat{\boldsymbol{k}}$ component of vorticity. At the boundary, we apply a far-field boundary condition, i.e. $\psi' = 0$, and

$$\left.\begin{aligned}
\frac{\partial}{\partial x}(a', b', c', z') = \boldsymbol{0} \quad \text{at } x = \pm L/2, \\
\frac{\partial}{\partial y}(a', b', c', z') = \boldsymbol{0} \quad \text{at } y = \pm L/2.
\end{aligned}\right\} \qquad (3.3g)$$

Here $\Omega = [-L/2, L/2] \times [-L/2, L/2]$ is our computational domain that is discretized into $n_x \times n_y$ grid points.

3.2. *Initial value calculations*

The time-dependent base state results in a non-orthogonal stability matrix, thus modal analysis may not capture the early-time dynamics appropriately. Therefore, we have employed non-modal analysis, solving initial value problems for numerical LSA to study the transient behaviour of the reactive displacements. This LSA serves as an efficient method to explore time-dependent linear systems in miscible VF (Tan & Homsy 1986; Matar & Troian 1999; Daniel, Tilton & Riaz 2013; Tilton, Daniel & Riaz 2013; Hota *et al.* 2015*b*; Pramanik, Hota & Mishra 2015). We solve the system of equations with the method of lines. We use the third-order Runge–Kutta method to solve the initial value problem for both base state and linearized perturbed equations (3.3*c*)–(3.3*f*), resulting from the discretization of spatial derivatives. Further, a highly efficient pseudospectral method hybridized by the compact finite difference method of sixth order is used to solve the Poisson equation (3.3*a*). In our study, we do not incorporate wavelength selection, while our LSA method does allow for wavelength selection (Hota *et al.* 2015*b*). Further, we perturb the base state around the interface where fastest growing perturbations are known to be localized (Ben *et al.* 2002; Hota *et al.* 2015*b*). We perturb the base state using a consistent set of random initial conditions around the interface as follows:

$$(a', b', c', z')(\boldsymbol{x}, t = 0) = 10^{-3} \begin{cases} (\sin(2\pi m_1), \sin(2\pi m_2), 0, \sin(2\pi m_1)), & |\boldsymbol{x}| = r_0, \\ (0, 0, 0, 0), & \text{otherwise.} \end{cases}$$
$$(3.4)$$

Here, m_1 and m_2 are random functions generating numbers between 0 and 1 which are kept consistent across all simulations. The remaining parameters used in LSA are mentioned

Parameters	dt	$n_x = n_y$	L	r_0	Pe
Value	10^{-4}	1025	1.5	0.075	3000

Table 1. Table showing the parameters used in the LSA.

in table 1. The numerical method is explained in detail in Sharma *et al.* (2023) and the references therein.

Since the base state is unsteady, we seek to analyse the temporal evolution of perturbations in the comparison of the base state (Shen 1961; Hota, Pramanik & Mishra 2015*a*). To do the same, we utilize the energy method approach and determine the normalized energy function with respect to the base state profile for both the perturbed concentration, α' and $\boldsymbol{u}'$:

$$R(t) = \frac{\displaystyle\int_{\Omega} \alpha'^2 + \boldsymbol{u}'^2 \, \mathrm{d}\Omega}{\displaystyle\int_{\Omega} \alpha_0^2 + \boldsymbol{u}_b^2 \, \mathrm{d}\Omega}, \tag{3.5}$$

where α' is the dummy variable for perturbed concentrations and $\alpha' \in \{a', b', c', z'\}$.

Further, we compute energy amplification, $E(t)$ by normalizing energy $R(t)$ with $R(t = 0)$ (Matar & Troian 1999) as

$$E(t) = \frac{R(t)}{R(t = 0)}. \tag{3.6}$$

Since we perturb the concentrations of the reactants initially, we use either a' or b' in the energy calculation in (3.5). In addition, it is reported that the temporal evolution of $\ln(E(t))$ is similar; hence, it makes no difference whether we choose a' or b' for the analysis (Sharma *et al.* 2023). We use a' and A_0 for the further computation of energy amplification. For unstable displacement, when perturbations amplify with time, $\ln(E(t))$ increases with time, while a monotonically decreasing profile of $\ln(E(t))$ is obtained for stable displacements. The transition in stability from stable to unstable displacement is depicted by a minimum in the $\ln(E(t))$ curve. We denote that time as the onset time when perturbations start to grow (Hota *et al.* 2015*a*).

It is noteworthy that the time domain is confined to $t = 1$, representing the duration over which our investigation is conducted. Hence, we analyse the stability of reactive displacement in transient time regimes only, not for asymptotic times. It has been observed that there exists a diffusive regime at later times for radial flows (Chui, De Anna & Juanes 2015; Verma *et al.* 2023). For non-reactive fluids, experimental observations indicate that the interface growth decelerates, scaling as $\sim t^{1/2}$ at later times, showing the existence of a diffusive regime as anticipated in stable displacements (Chui *et al.* 2015). It indicates the shutdown of overall flow instability. This phenomenon is reported as frozen fingers. Moreover, Verma *et al.* (2023) has reported the existence of frozen fingers for reactive fluids. Hence, the asymptotic analysis for reactive VF for radial flow is not required.

3.3. *Transient energy growth*

The system of (2.2) describes the reactive and non-reactive displacement both depending on the value of Da. For $Da = 0$, the system represents a non-reactive displacement where all the fluids are non-reactive in nature and follows the convection–diffusion equation. The viscosity profile is monotonic and is given by $\mu = \exp(R_b b)$ due to no product
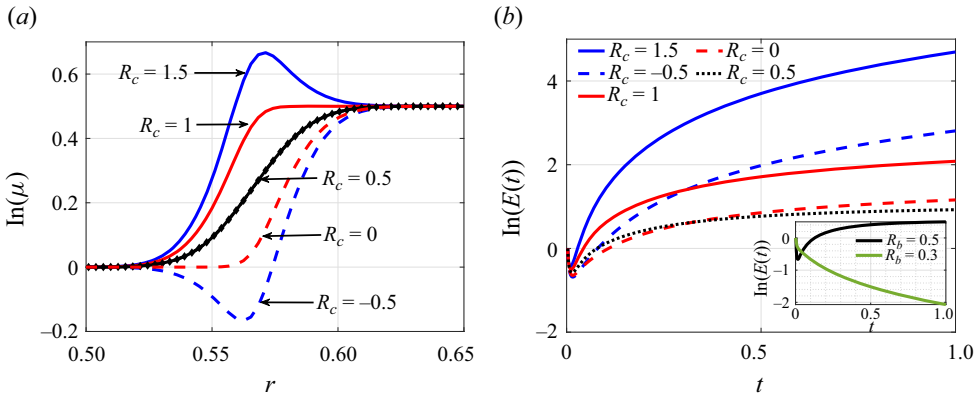
1000 A72-8

(a)

(b)

Figure 3. (a) Viscosity profile for $Da = 100$, $Pe = 3000$, $R_b = 0.5$ and various R_c. (b) Log energy amplification with time for $Da = 100$, $R_b = 0.5$ and various R_c showing unstable displacement. Inset: $\ln(E(t))$ of $R_b = 0.5, 0.3, Da = 0$.

formation, i.e. $c = 0$. Further, the monotonic viscosity profile may be modified in the presence of a chemical reaction when $Da \neq 0$. The viscosity profile for various R_c is shown in figure 3(a).

In the present study, we aim to compare the reactive and non-reactive displacement when the viscosity contrast, R_b, between displacing fluid A and displaced fluid B is the same. Further, for non-reactive fluids, it is reported that there exists a critical viscosity contrast for instability for radial flow (Sharma *et al.* 2020). Hence, we divide the reactive displacement into two categories depending on whether the corresponding non-reactive displacement is stable or unstable. First, we consider the reactive displacement when the corresponding non-reactive situation, that is, $Da = 0$, is stable and examine if the chemical reaction affects the flow stability. In the second category, we consider those types of reactions for which reactants already have an unfavourable viscosity contrast for instability. We examine how stability behaviour, such as the growth rate of perturbations and onset of instability, is affected by product formation. In order to evaluate the variation between reactive and non-reactive displacement, we must first review the stability of the non-reactive system before analysing the reactive displacement. We observe that $R_b = 0.5$ represents unstable displacement, while $R_b = 0.3$ corresponds to a stable displacement as explained below.

It can be verified that the flow is unstable for $R_b = 0.5$, $Da = 0$ as the $\ln(E(t))$ increases with time after obtaining a minimum as shown in the inset of figure 3(b). In the case of unstable displacement, the initial decrements in energy show the initial diffusion in the system, and instability takes some time to manifest. The minimum denotes the onset time of instability when instability appears. From the onset time, the convection starts to dominate the flow dynamics and the perturbation growth begins. In contrast, if we decrease the viscosity ratio between reactants to $R_b = 0.3$, the flow remains stable for the entire time domain as shown in the inset of figure 3(b) despite an unfavourable viscosity contrast. Thus, we have obtained two values of R_b showing that an increase in viscosity contrast leads to the transition in stability for the non-reactive situation. Now we analyse how the stability of the monotonic viscosity profile is influenced by varying R_c.

3.3.1. *Effect of R_c*

When we consider the non-reactive displacement, we have to deal only with a perturbed concentration that follows a linearized perturbed equation corresponding to

one convection–diffusion equation. While in the reactive case, we have to handle three perturbed concentrations that follow (3.3*c*)–(3.3*e*), and the complexity of the system analysis escalates. Therefore, it is absurd to compare the evolution of perturbed reactive or non-reactive concentrations directly. Additionally, we want to compare VF dynamics as a result of the modified viscosity profile, hence we find a value of R_c for which the corresponding viscosity profile is not modified in the presence or absence of the reaction.

When the product viscosity differs from that of the displacing fluid reactant *B*, i.e. $R_c \neq R_b$, the viscosity profile becomes either non-monotonic or remains monotonic but with steeper viscosity contrast as shown in figure 3(*a*) for $Da = 100$, $R_b = 0.5$ and various R_c. Due to the presence of all three fluids, Hejazi *et al.* (2010) has identified two mixed zones: the trailing and leading zones. The region occupied by the displacing reactant *A* and product *C* is defined as the trailing zone, while the region inhabited by displaced fluid, *B* and *C* is termed as the leading zone. The significance of defining these regions is that different viscosity contrast occurs in these two zones when $R_b \neq R_c$ and plays an individual role in determining the overall stability of the system. The viscosity contrast at the trailing zone is decided by the factor $R_c/2$ while $R_b - R_c/2$ determines the viscosity ratio at the leading zone (Hejazi *et al.* 2010; Verma *et al.* 2023). For $R_b = R_c = 0.5$, it is evident that $R_c/2 = R_b - R_c/2$, that is, the viscosity in both zones is the same. Thus, the viscosity contrast for $R_c = 0.5$ is monotonic, similar to that of $R_b = 0.5$ as shown in figure 3(*a*). Thus, when a chemical reaction alters the viscosity profile, this specific case of $R_c = 0.5$ can be used as a reference viscosity profile. For instance, if we compare the viscosity profile in figure 3(*a*), it is evident that the viscosity profile remains monotonic for $R_c = 0, 1$ but the reaction results in a non-monotonic viscosity profile for $R_c = 1.5, -0.5$. Even for the monotonic case, if we compare the profiles for $R_c = 0, 0.5, 1$, we can see that the viscosity profile at the trailing zone is steepened for $R_c = 1$, while it is steepened at the leading zone for $R_c = 0$. We analyse how this affects the onset of instability.

We have plotted the log energy amplification curve for various R_c with $R_b = 0.5$ in figure 3(*b*). For $R_c = 1$, the viscosity profile steepens at the trailing zone particularly and becomes flat at the leading zone where $R_b - R_c/2 = 0$. Due to this, the onset occurs early and the system exhibits more energy amplification for $R_c = 1$ than $R_c = 0.5$ despite the same endpoint viscosity contrast. Now we analyse the energy amplification for $R_c = 0$, where unfavourable viscosity contrast is shifted at the leading zone. The energy amplification for $R_c = 0$ is more than that of $R_c = 0.5$ at a later time only. However, at an early time, the energy amplification is less for $R_c = 0$, and hence the system is less destabilized than $R_c = 0.5$. It shows the significance of the location where the unfavourable viscosity contrast occurs and instability appears. Here, the viscously stable trailing zone stabilizes the system at early times. While the unstable, leading zone will be carried into effect late and the system destabilizes more when instability appears in the trailing zone. Thus, despite the same viscosity contrast in their unstable zone for $R_c = 0, 0.5, 1$ and $R_b = 0.5$, the system may attribute stability transition at a different time by varying unfavourable viscosity contrast locations.

Further, when $R_c = 1.5$ and $R_c = -0.5$, the viscosity profile becomes non-monotonic, resulting in unfavourable viscosity contrasts at the trailing and leading zones, respectively. Figure 4(*a*) shows the position of the *r*, at which the average reaction rate attains maximum, is the separator between the two zones. For $R_c = 1.5$ ($R_c = -0.5$), the leading (trailing) zone stabilizes and instability is expected to develop at the trailing (leading) zone. To illustrate this, we plot the perturbation profile for c' in polar coordinates at $t = 1$ for both $R_c = -0.5$ and $R_c = 1.5$ in figures 4(*b*) and 4(*d*), respectively. For $R_c = 0.5$, the viscosity profile is monotonic, and hence, the perturbation profiles are distributed symmetrically
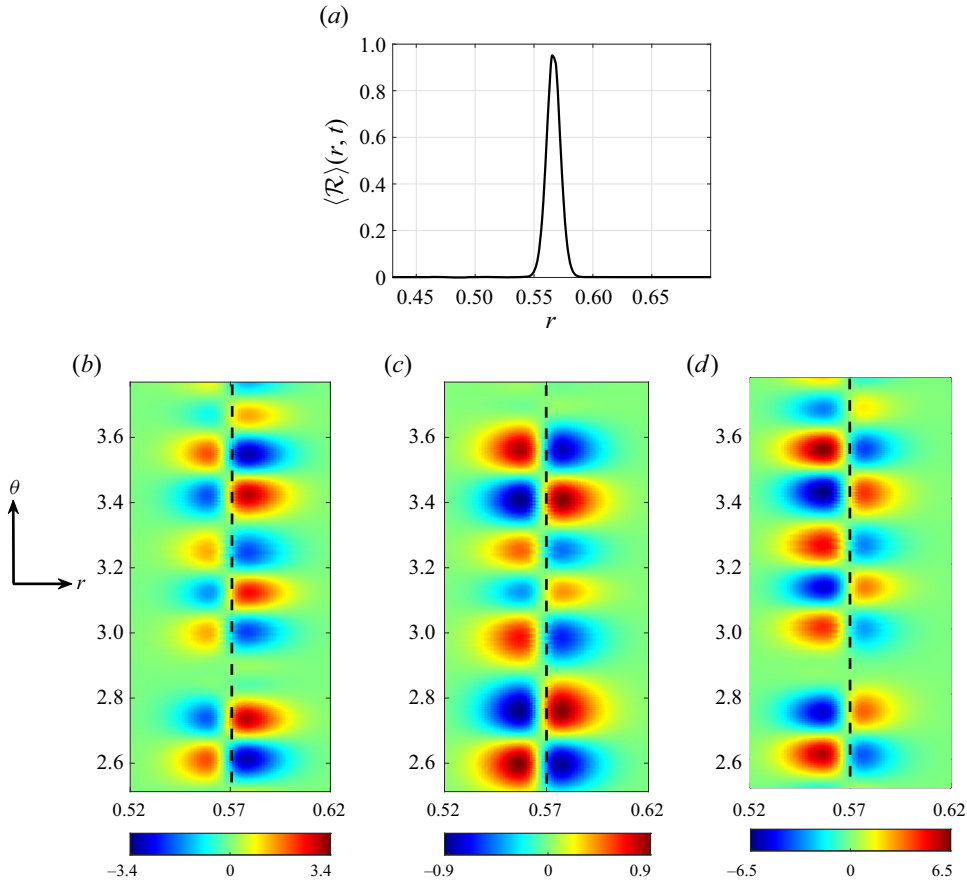
Figure 4. (*a*) Averaged reaction rate profile, $\langle \mathcal{R} \rangle (r, t) = (1/2\pi) \int_{r_0}^{R_0} \mathcal{R}(r, \theta, t) \, d\theta$ and $\mathcal{R} = DaA_bB_b$ for base state for $Da = 100$ and $Pe = 3000$. Cropped plot of perturbed concentration profile $C \, (10^4 \times c')$ for $Pe = 3000$, $Da = 100$, $R_b = 0.5$, (*b*) $R_c = -0.5$, (*c*) $R_c = 0.5$ and (*d*) $R_c = 1.5$ at final time $t = 1$ in polar coordinates. Here, the black-dashed line denotes the position where the reaction rate is maximum, as shown in (*a*).

in both mixing zones, as depicted in figure 4(*c*). In contrast, the presence of localized unstable zones leads to a more concentrated distribution of perturbation at the trailing (leading) zone when $R_c = 1.5$ ($R_c = -0.5$). Moreover, we plot perturbation profiles for a', b' and z' in Appendix A.

In the energy amplification plots in figure 3(*b*), $\ln(E(t))$ increases more for $R_c = 1.5$ than $R_c = -0.5$ depicting more amplified perturbations for $R_c = 1.5$ despite the same viscosity contrast at respective unstable zones. It can be concluded that the perturbations amplify more with enhanced energy amplification $\ln(E(t))$ with a higher growth rate of perturbations for an increased viscosity contrast, $|R_b - R_c|$ for any fixed R_b. This aligns with both the findings from the existing linear stability analysis (Hejazi *et al.* 2010) and NLS (Sharma *et al.* 2019; Verma *et al.* 2023) qualitatively. The NLS indicate that as the viscosity ratio increases, the onset time of instability decreases, which leads to rigorous VF patterns (Sharma *et al.* 2019; Verma *et al.* 2022, 2023). In addition, the mixing phenomena are enhanced (Verma *et al.* 2023).

Further, it can be seen that for each pair $|R_c - R_b|$, despite the identical viscosity contrasts, the system exhibits a greater energy amplification for the case $R_c - R_b > 0$ than
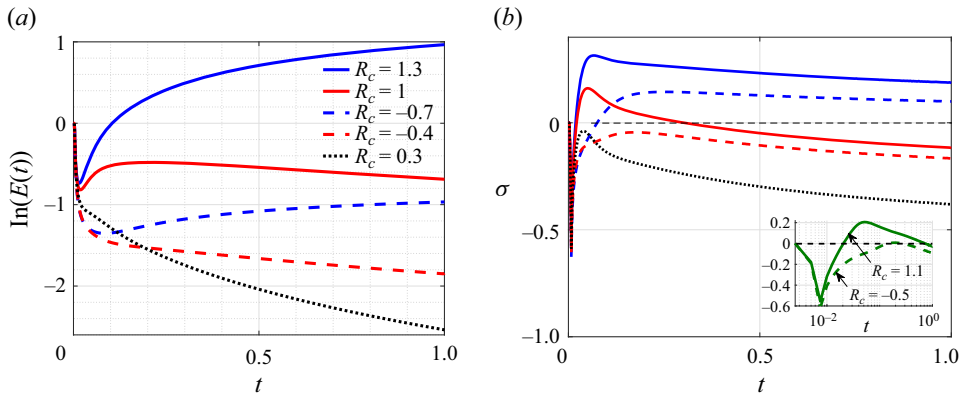
Figure 5. (*a*) Log energy amplification and (*b*) growth rate with time for $Da = 100$, $Pe = 3000$, $R_b = 0.3$ and various R_c showing unstable displacement. Inset: growth rate for $R_c = 1.1, -0.5$ showing an unstable and stable displacement, respectively, despite the same viscosity contrast $|R_b - R_c|$.

the corresponding case, $R_c - R_b < 0$ as shown in figure 3(*a*). This raises the question of why the perturbations amplify more when the unstable zone is situated at the trailing zone in contrast to the leading zone despite the viscosity contrast being the same ($|R_c - R_b|$). The velocity profile holds the responsibility for this property of radial flow. The velocity magnitude decreases with the radial distance, which provides more convection to the trailing zone than the leading zone (Sharma *et al.* 2019; Verma *et al.* 2022). Moreover, it hints at the asymmetry in the (R_b, R_c) phase plane along the non-reactive region, $R_c = R_b$. We explore the asymmetry in the (R_b, R_c) phase plane by taking corresponding stable non-reactive situations and finding the corresponding R_c parameters that destabilize the flow. In the inset of figure 3(*b*), the flow is shown stable for $R_b = 0.3$. If the reaction generates a product with enough high or less viscosity that makes the viscosity profile non-monotonic and one of the zones becomes viscously unstable, the flow may become unstable. We will next investigate these situations.

In figure 5(*a*), the flow is shown stable for some range of R_c, including $R_c = 0.3$ and on further increment of viscosity ratio, the system becomes unstable. For the viscosity contrast $|R_c - R_b| = 1$ ($R_c = 1.3, -0.7$), the flow is unstable as $\ln(E(t))$ increases with time after attaining a minimum, while the flow is stable for $R_c = -0.4$. It is interesting to note that when $R_c = 1$, the system behaves inconsistently. Following a minimum, $\ln(E(t))$ rises at first, then starts to fall as the energy amplification increases to saturation. For better visualization, we compute the growth rate as in Tan & Homsy (1987):

$$\sigma = \frac{t}{2E}\frac{\mathrm{d}E}{\mathrm{d}t}. \tag{3.7}$$

Evidently, the growth rate of perturbations is negative for $R_c = 1$ at later times after onset; there is a decay in perturbation growth as shown in figure 5(*b*). The positive growth rate indicates that the perturbations grow after onset time. However, the unfavourable viscosity contrast at the trailing zone is not enough to sustain the growth of perturbations for a longer time and it starts to decrease again. A similar transition in stability is observed in the literature (Hota & Mishra 2018) for rectilinear flow. There, the secondary instability appears at late times after the first minima in $\ln(E(t))$. The uniform velocity in the rectilinear displacement constantly feeds the flow and is responsible for this transition. However, in our case, the flow velocity reduces with radial distance and at the unstable zone with time. As a result of this, once the flow is stabilized, convection is not able to
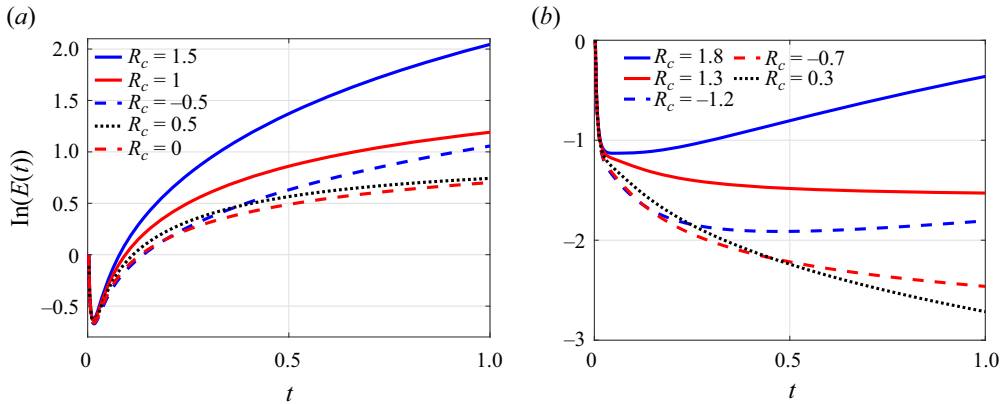
Figure 6. Log energy amplification with time for $Da = 10$, $Pe = 3000$, (a) $R_b = 0.5$, (b) $R_b = 0.3$ and various R_c showing unstable displacement.

induce instability again. Hence, the flow is considered stable for $R_c = 1$. In conclusion, we have obtained a stable zone for a range of R_c when the corresponding non-reactive displacement is stable. In addition, we obtain such values of R_c where the flow is unstable when $R_c - R_b > 0$ ($R_c = 1.1$) while stable for the corresponding case $R_c - R_b < 0$ ($R_c = -0.5$) showing asymmetry in the (R_b, R_c) phase plane. We discuss this in detail in § 4. The growth rate of perturbations is negative for $R_c = -0.5$, while the system shows a positive growth rate after onset in perturbation evolution for $R_c = 1.1$. Now, the question arises of how changing the reaction rate, Da, influences the stability of the reactive system, regardless of whether the system is initially stable or unstable.

3.4. *Effect of Da*

When reactants are isoviscous, $R_b = 0$, NLS have shown that the onset of instability gets delayed and the critical viscosity ratio for instability is exceeded with lowering Da (Sharma *et al.* 2019). Here, we explore the effect of Da when $R_b \neq 0$. From the comparison of the figures 3 and figure 6(a), it can be observed that the $\ln(E(t))$ is less for $Da = 10$ after onset time. It happens as a result of the reduced amount of product decreasing the viscosity and thus the viscosity gradient, resulting in slower growth of perturbations. Furthermore, if we compare energy amplification for $R_b = 0.3$, $Da = 100, 10$ and various R_c as in figures 5 and 6(b), the stable range of R_c increases for decreased Da. Flow is unstable for both the parameters $R_c = 1.3, -0.7$ when $Da = 100$, but for $Da = 10$, these parameters belong in the stable range of R_c for $R_b = 0.3$.

We have now covered the cases when the viscosity profile is modified due to the formed product having viscosity contrast with reactants. However, there is another case when product viscosity is identical to displacing fluid reactant B, i.e. $R_b = R_c$ regardless of Da, the viscosity profile remains the same as the corresponding non-reactive situation, $(R_b, Da = 0)$ (Nagatsu & De Wit 2011). For such cases, we claim that no change in the flow stability occurs when $R_b = R_c$ provided the flow is stable with or without the reaction, for instance, when $R_b = 0.3$. No change in perturbation growth or energy amplification should be observed when the system is already unstable for corresponding non-reactive situations $R_b = 0.5$ for changing Da. Instead of reactant A, we show energy amplification for dye concentration. Since dye concentration follows the convection–diffusion equation
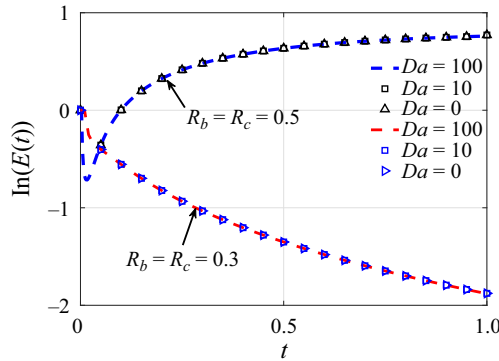
Figure 7. Log energy amplification with time for $R_b = R_c = 0.5$, 0.3 and various Da, and $Pe = 3000$. Here, all the curves for different Da and fixed viscosity contrast are merged.

as followed by A when $Da = 0$, considering z allows us to examine the stability of the parameter $R_b = R_c$ for varied Da ranging from $Da = 0$ to $Da = 100$.

From figure 7, it can be concluded that the stability is unaffected by a chemical reaction when $R_b = R_c$ as energy amplification regardless of whether the system is stable or unstable before the reaction.

4. Nonlinear simulations

To support the fact that the results of LSA are not a consequence of linearized equations, we perform NLS for the VF instability on the system of equations given in (2.2). We utilize a highly efficient pseudospectral method hybridized with the compact finite difference method to solve the coupled nonlinear system of partial differential equations. We decompose the velocity into two parts with rotational velocity ($\boldsymbol{u}_{rot}$) and potential velocity, ($\boldsymbol{u}_{pot}$) that defines the unperturbed flow as given in (2.4b). In addition, we define the rotational component to capture the instability by introducing the stream function as

$$\boldsymbol{u} = \boldsymbol{u}_{pot} + \boldsymbol{u}_{rot}, \quad \boldsymbol{u}_{rot} = \left(\frac{\partial \psi}{\partial y}, -\frac{\partial \psi}{\partial x} \right), \quad (4.1a)$$

$$\nabla^2 \psi = -\omega, \quad \omega = R_c \left(v \frac{\partial c}{\partial x} - u \frac{\partial c}{\partial y} \right) + R_b \left(v \frac{\partial b}{\partial x} - u \frac{\partial b}{\partial y} \right). \quad (4.1b)$$

We solve Poisson equations (4.1b) by applying Fourier sine expansion to solve $x-$ derivative and discretize the $y-$ derivative with the compact finite difference of sixth order. Further, the initial value problem in (2.2)(b–e) is solved by the third-order Runge–Kutta method with adaptive time steps satisfying the Courant–Friedrichs–Lewy condition. The remaining details are explained in Sharma *et al.* (2019) and Verma *et al.* (2022).

To track the instability, we plot the dye concentration profile for $R_b = -1, 1, Da = 100$, $Pe = 3000$ and for various R_c at the final time $t = 1$ in figure 8. It is evident that the flow is unstable for $R_b = 1$ irrespective of R_c. In contrast, the flow is stable for $R_b = -1$, and we obtain a range of R_c where a transition can be observed in flow stability. For non-reactive flow, the flow is stable for $R_b = -1$ due to a monotonically decreasing viscosity profile. A chemical reaction generates a product having some viscosity contrast with reactants and the viscosity profile becomes non-monotonic with extremum. However, we obtain stable
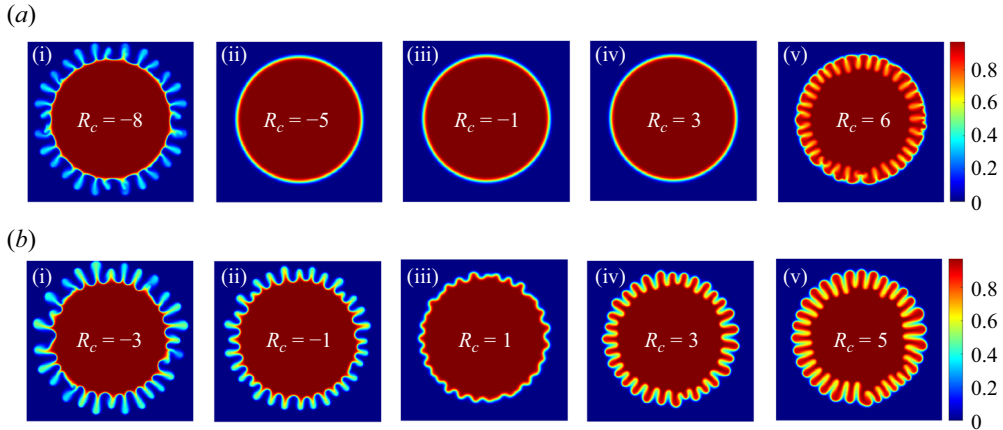
(*a*)

(*b*)

Figure 8. Dye concentration profile for $(Da, Pe) = (100, 3000)$, (*a*) $R_b = -1$ and (*b*) $R_b = 1$ and various R_c at final time $t = 1$.

displacement when $R_c = 5, -3$ and unstable when $R_c = -8, 6$. Evidently, reaction can induce instability but it requires a critical viscosity contrast for instability. This supports the findings presented by LSA in figure 3(*b*), suggesting that instability persists in reactive flow if the equivalent non-reactive system is unstable. Furthermore, upon comparing figure 8(*a* i,*b* i) and figure 4(*b*) obtained from NLS and LSA, respectively, we note that instability predominantly develops in the leading zone when $R_c < R_b$. Similarly, instability appears in the trailing zone when $R_c > R_b$, as evidenced by LSA in figure 4(*d*) and NLS in figure 8(*a* v,*b* v). When $R_c = R_b$, the instability is not localized in any specific zone, as shown by LSA in figure 4(*d*) for $R_b = R_c = 0.5$ and by NLS in figure 8(*b* iii) for $R_b = R_c = 1$. Additionally, a comparison between figures 5(*a*) and 8(*a*) illustrates a stable range of R_c in the (R_b, R_c) phase plane for a constant R_b in the corresponding stable non-reactive system.

The experimental findings of Riolfo *et al.* (2012) confirm our results. They have conducted experiments where a highly viscous fluid, polyacrylic acid (PAA), displaces a less viscous fluid, sodium hydroxide (NaOH), leading to a reaction PAA + NaOH → SPA + H$_2$O, resulting in the formation of a highly viscous product, salt sodium polyacrylate (SPA). In this scenario, the viscosity ratios were characterized by $R_b = \ln(\mu_B/\mu_A) = -6.7685$ and $R_c = \ln(\mu_C/\mu_A) = 1.495$, with viscosities of PAA, NaOH and SPA are 870 centipoise (cp), 1 cp and 3880 cp denoted as μ_A, μ_B and μ_C, respectively. This value of R_b and R_c lies in Zone III in (R_b, R_c) phase plane. We have explained the zones in Appendix C. The non-monotonic viscosity profile, exhibiting maxima within the reaction zone, induces instability in the trailing zone as shown in figure 5(*b*) from Riolfo *et al.* (2012). Further, they present another experiment where a highly viscous fluid, SPA, displaces a less viscous fluid, an aqueous mixture of hydrogen chloride and glycerol (HCl), resulting in a reaction SPA + HCl → PAA + NaCl and generating a less viscous product (PAA). In this case, the viscosity ratios were $R_b = -4.3745$ and $R_c = -5.0676$, with viscosities of 794 cp, 10 cp and 5 cp for PAA, HCl and SPA, respectively. This value of R_b and R_c lies in Zone II in (R_b, R_c) phase plane as explained in Appendix C. Again, the non-monotonic viscosity profile within the reaction zone led to instability and the formation of fingering patterns due to the increment in viscosity at the leading zone, as shown in figure 5(*b*) from Riolfo *et al.* (2012).

The viscosity gradient at the trailing and leading zone is decided by $R_c/2$ and $R_b - R_c/2$, respectively. The instability is anticipated to occur at the trailing zone if $R_c > 0$. Thus, we determine the critical viscosity ratio at the leading zone so that the diffusion can weaken the responsible forces due to convection in the trailing zone. In another way, we find a critical R_b that can stabilize the flow. Similarly, if $R_c < 0$, then the flow can be destabilized for increasing viscosity gradient, $R_b - R_c/2 > 0$ at the leading zone. Hence, finding a critical R_b for a given R_c for the computational study will be convenient. To determine instability, we measure the deformation of the interface by interfacial length in the dye concentration (Mishra, Martin & De Wit 2008; Sharma *et al.* 2019). It is calculated by $I(t) = \int_\Omega |\nabla z| \, d\Omega$. For stable displacement, interfacial length follows the relation $I_0(t) = 2\pi\sqrt{r_0^2 + t/\pi}$ (Sharma *et al.* 2020). Evidently, for a deformed interface, the interfacial length increases, and if interfacial length, $I(t)$ coincides with $I_0(t)$ for the entire time domain, that parameter can be considered as stable displacement. We define the flow as unstable when the relative difference in interfacial length is greater than zero, that is, $\Delta I = (I - I_0)/I_0 > 0$.

A phase plane (R_b, R_c) is presented in figure 9 where the solid curves show critical viscosity ratio (R_b, R_c) for instability for each *Da* and the region below the curve is stable and above the curve is the unstable region. It can be observed that if reactants have favourable viscosity contrast, i.e. $R_b < 0.66$, then two critical R_c can be determined that destabilize the flow for a given reaction rate. It happens when a chemical reaction introduces a non-monotonic viscosity profile and persuades convection and diffusion to compete, as suggested by LSA results. We obtain a range of R_c when $R_b < 0.66$ corresponds to the stable flow. This range contracts for increasing R_b and vanishes when $R_b = R_c = 0.66$. The viscosity contrast between reactants, $R_b = 0.66$, is the maximum R_b for which flow is stable before the reaction and the reaction may alter the stability. Moreover, if reactants have viscosity contrast, $R_b > 0.66$ and the stability will not be changed by the reaction. It exhibits the limitations of the influence of reaction on the stability of the system. It is evident in figure 9 that the region around $R_c = 0.66$ is stable for all values of *Da*. This is the *Da*-independent critical regime that we have reported for radial VF.

The value of viscosity ratio $(R_b, R_c) = (0.66, 0.66)$ is of special interest for us. For $(R_b, R_c) = (0.66, 0.66)$, the viscosity profile is monotonic and identical to its inherent viscosity profile in corresponding non-reactive situations. Now, we claim that the viscosity ratio when $R_b = 0.66$ is also the critical viscosity ratio for the non-reactive fluids. For non-reactive fluids, Sharma *et al.* (2020) have established a scaling relation between Péclet number *Pe* and critical log-mobility ratio R_b numerically:

$$R_b = \alpha(r_0)Pe^{-\beta}, \quad \alpha = 30(1 + 10r_0). \tag{4.2}$$

Here β lies under confidence bounds $(0.52, 0.59)$ and critical parameters (R_b, Pe) lies on the boundary that is given by $R_b = \alpha(r_0)Pe^{-0.55}$. Since (4.2) is determined numerically and has theoretical and experimental support, it provides a fair opportunity to compare reactive displacement with the corresponding non-reactive displacement in the context of stability. In all the simulations, we have considered $Pe = 3000$ and $r_0 = 0.075$, if we put the same value of *Pe* and r_0 in (4.2), we obtain the critical $R_b = 0.642$. In addition, if we find the range for this critical viscosity ratio in the 95 % confidence bound, we obtain $R_b \in (0.466, 0.817)$. The obtained critical viscosity R_b for the reactive case lies in the range $R_b \in (0.466, 0.817)$ which also contains the calculated viscosity ratio, $R_b = 0.642$ for the non-reactive displacement.
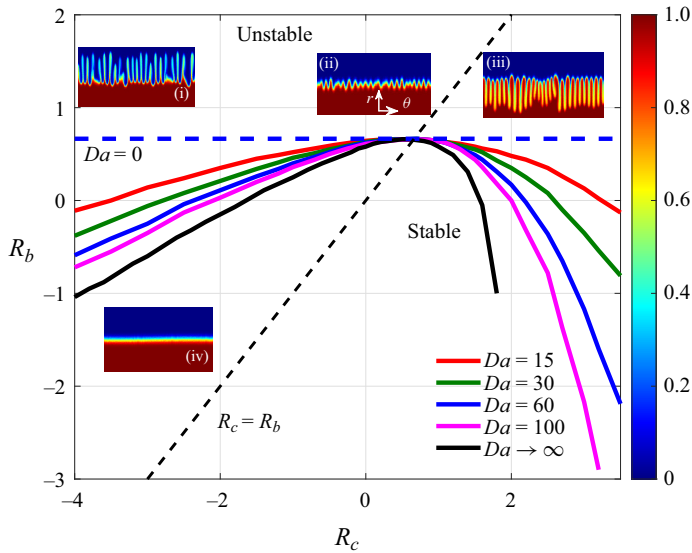
Figure 9. The (R_b, R_c) phase plane for $Pe = 3000$, various Da along with $Da \to \infty$. Inset: dye concentration profile for $R_b = 1$, (i) $R_c = -3$, (ii) $R_c = 1$, (iii) $R_c = 5$ showing unstable displacement and (iv) $R_b = R_c = 0$ showing stable displacement in polar coordinates.

Though the viscosity profile is modified only when $R_b \neq R_c$, thus the effect of product viscosity R_c on stability can be compared along the line $R_b = R_c$ whether the reaction increases or decreases the viscosity of the system. The specific value $(R_b, R_c) = (0.66, 0.66)$ distinguishes the stability behaviour of reactive and non-reactive displacement. Furthermore, during the LSA analysis, we noticed an asymmetry in the (R_b, R_c) phase plane along the line $R_c = R_b$. Despite having the same viscosity contrast $(|R_c - R_b|)$, perturbations exhibit a higher growth rate when $R_c > R_b$ compared with the opposite case, $R_c < R_b$ as in figures 3(b) and 6(a). The critical viscosity contrast is greater when the reaction decreases viscosity, i.e. $R_c < R_b$, than in the opposite case, $R_c > R_b$, if a system is stable for the corresponding non-reactive case ($R_c = R_b$) as shown in figures 5 and 6(b). Similarly, in the (R_b, R_c) phase plane obtained from NLS, we observe asymmetry along the line $R_c = R_b$. The critical R_b decreases more significantly when $R_c > 0.66$ compared with when $R_c < 0.66$. To visualize more about this asymmetry, we have plotted a phase plane between $R_c/2$ and $R_b - R_c/2$ that shows viscosity contrast at trailing and leading zone in figure 10(a). It can be observed that if the trailing front is stable, the critical viscosity contrast for instability, $R_b - R_c/2$ is more than $R_c/2$ if the leading front is stable. The asymmetry is a consequence of the spatially dependent base state velocity profile. When $R_c < 0.66$, the instability appears at the leading zone due to steeper viscosity contrast while the trailing zone stabilizes the flow. On the other hand, when $R_c > 0.66$, the instability appears at the trailing zone for the same viscosity contrast at the unstable zone. If we compare both R_c values for the same R_b maintaining the viscosity gradient $|R_c - R_b|$, the driving force provided by convection is more efficient at the trailing than at the leading zone. Consequently, the critical viscosity contrast to trigger instability at trailing zone $R_c/2$ is less than the critical viscosity ratio, $R_b - R_c/2$, to trigger the instability at the leading zone. Similar asymmetric behaviour is observed in Sharma *et al.* (2019). A higher viscosity ratio is required for instability when the reaction produces a less viscous product for $R_b = 0$ compared with when the product is highly viscous.
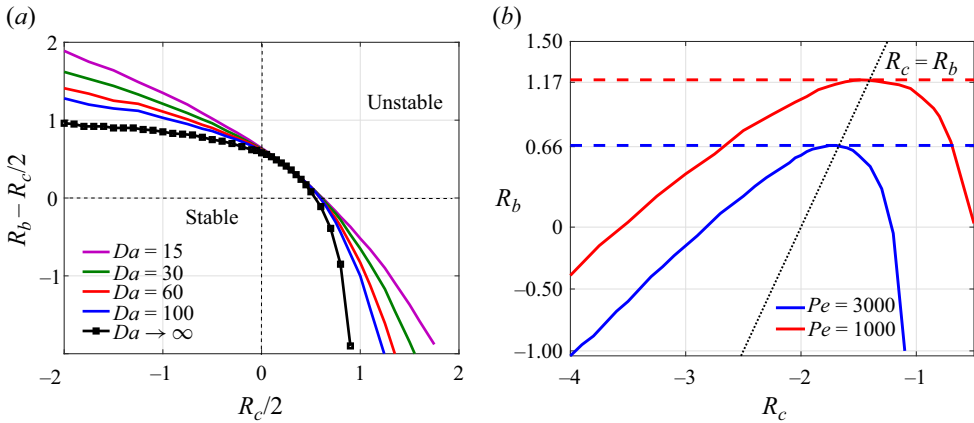
Figure 10. (*a*) Phase plane between the viscosity ratio at trailing and leading zone, $R_c/2$ and $R_b - R_c/2$ for $Pe = 3000$ and various Da. (*b*) The (R_b, R_c) phase plane for $Pe = 3000, 1000$ for $Da \to \infty$. Here below the curve is a stable region, and above the curve is an unstable region. Here the dashed lines correspond to the non-reactive case $Da = 0$ for $Pe = 3000$ (blue) and $Pe = 1000$ (red).

4.1. *Effect of Da and Pe (Da $\to \infty$)*

It is reported that the stable region exists for all moderate ranges of Da, and the width of the interval of stable R_c decreases with Da when $R_b = 0$ (Sharma *et al.* 2019). Interestingly, the stable region even exists for $Da \to \infty$ when $R_b = 0$ (Verma *et al.* 2022). When we increase Da, more product is formed that enhances the viscosity of the system as in (2.3), leading to an enhanced viscosity contrast and a higher growth rate of perturbations in the system as predicted by LSA and illustrated in figures 3(*b*), 5 and 6. Hence, the critical viscosity ratio decreases for higher Da as shown in figures 5, 6(*b*) and 9. However, the existence of the critical viscosity contrast is shown only for the particular case, $R_b = 0$. It will be intriguing to examine whether that critical viscosity occurs or identify the range of R_c that corresponds to stable displacements when $R_b \neq 0$. To investigate the same, we have performed simulations for a wide range of Da, including the limiting case $Da \to \infty$. For an instantaneous reaction, $Da \to \infty$, the reaction front occurs in an infinitesimally small region. This replicates an ideal situation where reactants are fully consumed at the reaction front as soon as the reactants meet, i.e. $a \to 0$, $b \to 0$ at the reaction front. The concept of the trailing zone and the leading zone is also based on this ideal situation $Da \to \infty$. As the trailing zone is only occupied by fluid A and C, and the leading zone is occupied by fluid B and C, in order to perform simulations for $Da \to \infty$, we rearrange our system of governing equations as in Verma *et al.* (2022), Nagatsu & De Wit (2011) and Michioka & Komori (2004) as follows:

$$\frac{\partial h}{\partial t} + \boldsymbol{u} \cdot \nabla h = \frac{1}{Pe} \nabla^2 h, \tag{4.3a}$$

$$(a, b, c) = \begin{cases} (0, 1 - 2h, h), & h < 0.5, \\ (-1 + 2h, 0, 1 - h), & h \geq 0.5. \end{cases} \tag{4.3b}$$

In figure 9, we have plotted the critical (R_b, R_c) curves for various Da. The stable zone in the (R_b, R_c) phase plane contracts for increasing Da but does not vanish even when $Da \to \infty$. It can be verified from a recent article (Kim *et al.* 2021) for the asymptotic limit of Pe and Da. For $R_b = 0$, it is reported that the minimum viscosity contrast to induce

1000 A72-18

the instability ($|R_c|$) is more, if the reaction generates a less viscous product ($R_c < 0$) than a high viscous product ($R_c > 0$). Further, the stable region in the Da–R_c phase plane along the line $R_c = 0$ becomes less symmetric with Da (Sharma *et al.* 2019). We observe the same for the case when $R_b \neq 0$. The stable region in the (R_b, R_c) phase plane becomes asymmetric for increasing Da around the line $R_c = R_b$. In addition, if we consider $Da = 0$, the stable region is obtained as $R_b < 0.64$, and the remaining region in the (R_b, R_c) phase plane is an unstable zone. Further, the viscosity profile is monotonic in the neighbourhood of $R_b = R_c$, and it is identical for each Da. Thus, the VF dynamics remain unchanged, and for this particular viscosity, all (R_c, R_b) curves showing the critical viscosity contrast are merged for various Da in the neighbourhood of $R_b = R_c$. This can be confirmed by both LSA and NLS as shown in figures 7 and 9, respectively. Thus, the reaction affects the stability of the flow, but the inherent non-reactive system equally contributes to the instability. There exists a region in the (R_b, R_c) phase plane that is preserved and unaffected by the reaction. This illustrates that the reaction is able to influence the stability of the system and may destabilize the initially stable system, for some values of R_c only.

Further, it can be observed that if we increase the value of r_0, it leads to weaker convection even at the initial time (Sharma *et al.* 2020). Consequently, the critical viscosity contrast required to trigger instability also increases for larger r_0 as stated in (4.2), and this holds for reactive fluids as well. In the phase plane (R_b, R_c) illustrated in figure 9, the maximum critical value of R_b required to induce instability increases with the increment of r_0, following the relationship (4.2). Below this maximum value of R_b, the stable range of R_c expands with an increase in r_0 for each R_b.

Finally, we check the effect of Pe on the stability of the system for given other parameters (Da, R_b, R_c). The Pe number definition suggests a tuning between the flow rate and diffusion coefficient. In another way, it decides the competition between forces due to convection and diffusion, and flow gets stabilized for decrements in Pe as diffusion works as a stabilizing factor. It is already reported that the stable region in the R_c–Da plane widens for decreasing Pe. However, the qualitative behaviour shown by the critical R_c–Da curves remains preserved for varying Pe (Sharma *et al.* 2019). To understand the effect of Pe on the VF dynamics when $R_b \neq 0$, we have fixed Da by $Da \to \infty$ and performed simulations for $Pe = 3000, 1000$. For $Pe = 1000$, the stable zone widens, and critical (R_b, R_c) increases to trigger the instability as in figure 10(*b*). Also, we can examine the critical viscosity ratio obtained in the case $R_b = R_c$ for that VF dynamics gets unaffected by chemical reaction for $Pe = 1000$. The critical viscosity ratio for non-reactive displacements is found around $R_b = R_c = 1.17$ for $Pe = 1000$, is the same value as computed from (4.2) for $Pe = 1000$ and r_0.

5. Conclusion

Reactive displacements in a porous medium are encountered in several transport phenomena that affect the productivity of the process, as the chemical reaction can alter the physical properties at the fluid–fluid interface. The presented problem is motivated as the generated product modifies the viscosity profile that affects the overall stability of the system. In this manuscript, we address the stability of a reactive system $A + B \to C$ in a porous medium subjected to VF instability, exploring a range of (R_b, R_c) through LSA. We discuss how the product viscosity of the inherent system influences the temporal evolution of the perturbations.

The LSA predicts that the modified viscosity contrast, i.e. $R_c \neq R_b$ stimulates the growth rate of perturbations. This leads to an earlier onset of instability and a higher growth rate of perturbations if the flow is already unstable without the reaction. These results agree with

the experimental studies (Nagatsu *et al.* 2007, 2009) as the reaction enhances the instability for radial flow. On the other hand, if the corresponding non-reactive displacement is stable, such chemical reactions can be categorized into two parts based on product viscosity, R_c. For a given reaction rate, *Da*, we can find a range of reaction types, R_c, including $R_c = R_b$, which correspond to the stable flow. In such reactive displacement, the altered viscosity profile is not enough to trigger instability. The system becomes unstable for the remaining reaction types R_c. Another conclusion that can be drawn from the LSA is that the system exhibits an early onset time and more amplified perturbations when induced by a high viscous product generation rather than a less viscous product. Moreover, such reactive displacements show a higher growth rate of perturbations if we increase *Da*. Meanwhile, the stable range of R_c contracts if the corresponding non-reactive displacement is stable. Also, some reactions exist where product viscosity is the same as the reactant, B, $R_c = R_b$, and thus, the stability of the system remains unaltered after the reaction regardless of *Da*.

Further, we perform NLS to determine the critical viscosity ratio (R_b, R_c) exhibiting instability in reactive displacement for a given *Da* and *Pe*. We provide sufficient data to determine the stability of the reactive displacement. We present a (R_b, R_c) phase plane separated by critical viscosity ratio for instability into the stable and unstable regions for the entire range of *Da* and various *Pe* explored. The importance of each parameter in determining the stability of the system is explained by the phase plane. The stable region in the (R_b, R_c) phase plane reduces for increasing *Da* and *Pe* but never completely disappears.

Our findings contribute to understanding the interaction between chemical reactions and VF dynamics. Further, the study has implications for various chemical-enhanced oil recovery mechanisms to reduce residual oil and increase oil production in reservoirs. Strategies such as controlling the mobility ratio (Green *et al.* 1998; Weidong *et al.* 2017; Sun *et al.* 2019), reducing interfacial tension (Sedaghat *et al.* 2016) and enhancing miscibility between displaced and displacing fluids (Jiang, James & Mojarab 2020) are fundamental mechanisms in enhanced oil recovery processes (Fani *et al.* 2022). Moreover, the reactive VF can help improve the sweep efficiency of injected CO_2, ensuring that it contacts more of the reservoir rock and displaces more of the resident fluids (e.g. oil or brine) (Sainz-Garcia *et al.* 2017; Lei & Luo 2021). This can lead to more effective CO_2 storage and reduced residual trapping of CO_2. In this regard, we establish a relation between critical viscosity ratios R_b and R_c to trigger the instability. Further, by adjusting the reaction rate *Da* and flow rate *Pe*, it is possible to achieve an optimum mixing depending on whether the flow is stable. Moreover, if the flow is stable, a transition in stability can be obtained by varying *Da* and *Pe* as per the application. For instance, instability is a suitable choice to increase fluid miscibility in chemical flooding during enhanced oil recovery.

Declaration of interest. The authors report no conflict of interest.

Author ORCIDs.
- Priya Verma https://orcid.org/0000-0002-2889-3205;
- Vandita Sharma https://orcid.org/0000-0002-9348-2410;
- Ching-Yao Chen https://orcid.org/0000-0002-3971-7995;
- Manoranjan Mishra https://orcid.org/0000-0001-9933-5828.

Flow inputs	k (s^{-1})	a_0 (mole m^{-3})	Q (m^2 s^{-1})	r_0 (m)	$Da = r_0^2 k a_0 / Q$
Values	[0.011, 0.049]	[0.004, 0.012]	[0.64, 770] $\times 10^{-9}$	0.002	[0.0003, 3.675]

Table 2. The parameters and corresponding values used in the experimental study from Nagatsu *et al.* (2009).

Appendix A. Choice of characteristic length scale

For the non-dimensionalization of the spatial vector, x, we can utilize either $\sqrt{\kappa}$, $\sqrt{Qt_f}$ or r_0. Despite several choices, determining an appropriate length scale has been a challenge. Previous works by Tan & Homsy (1987) utilized $\sqrt{\kappa}$ as a length scale due to the absence of an explicit length scale for non-reactive fluids. Further, if we consider r_0, a_0 and μ_0 as the characteristic scale for length, concentration and viscosity, the quantities can be non-dimensionalized as

$$x = \frac{\tilde{x}}{r_0}, \quad u = \frac{\tilde{u}}{Q/r_0}, \quad t = \frac{\tilde{t}}{r_0^2/Q}, \tag{A1a–c}$$

$$(a, b, c) = \frac{(\tilde{a}, \tilde{b}, \tilde{c})}{a_0}, \quad \mu = \frac{\tilde{\mu}}{\mu_0}, \quad p = \frac{\tilde{p}}{Q\mu_0/\kappa}, \tag{A2a–c}$$

where r_0 is the initial radius of a circular region filled by fluid A. Following this non-dimensionalization, the definition of Péclet number (Pe) remains the same as mentioned in the previous studies (Tan & Homsy 1987; Nagatsu *et al.* 2007; Sharma *et al.* 2019), i.e. $Pe = Q/D$. While the Da formulation will be altered as

$$Da = \frac{\text{hydrodynamic time scale}}{\text{reactive time scale}} = \frac{r_0^2/Q}{1/ka_0}. \tag{A3}$$

If we substitute the values from an experimental study performed by Nagatsu *et al.* (2009) and determine the range of Da, it varies between 0.0003 to 3.675 (as given in table 2). However, Nagatsu *et al.* (2009) obtained an extensive range of Da, varied from 1.4 to 64. Clearly, the Da range we obtain from this non-dimensionalization does not correspond with the findings of Nagatsu *et al.* (2009). Hence, It is apparent that r_0 may not be an appropriate selection for a characteristic length scale for such a reactive flow.

In our study, we define the length scale as $\sqrt{Qt_f}$ (Sharma *et al.* 2019). This choice offers practical advantages as it enables us to confine our temporal domain, given that the fingering pattern develops in the diffusive regime in later stages, contingent upon the Péclet number (Pe) (Chui *et al.* 2015; Verma *et al.* 2023).

Appendix B. Perturbation profile for a', b' and z'

We have plotted the density plot of perturbation for all the perturbed concentrations, a', b' and z' in figure 11. Given that the concentrations of base state reactants A and B are localized in the downstream and upstream mixing zones, respectively. In contrast, the perturbed z' remains unlocalized in any mixing zone, resembling the base state profile. Additionally, we observe a quadruple structure for the perturbed concentration c' in figure 4, influenced by the perturbed concentrations of reactants b' and a', as described in (3.3).
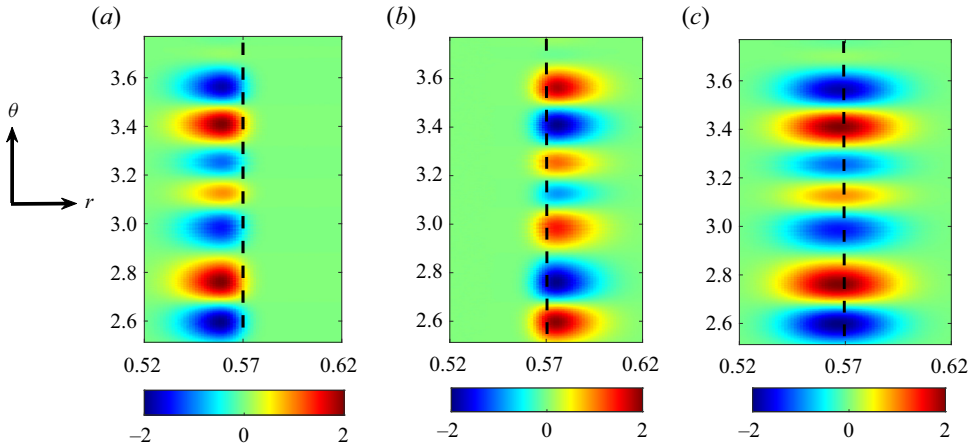
1000 A72-21

Figure 11. Cropped plots of perturbed concentration of A, B and dye for $Da = 100$, $Pe = 3000$, $R_b = 0.5$ and $R_c = 0.5$ at final time $t = 1$ in polar coordinates. Here, (a) $10^4 \times a'$, (b) $10^4 \times b'$ and (c) $10^4 \times z'$.
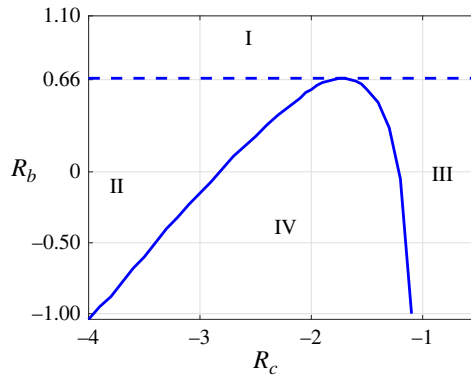

Figure 12. The (R_b, R_c) phase plane for $Pe = 3000$ for $Da \to \infty$.

Appendix C. Stable and unstable zones in (R_b, R_c) phase plane

For a given Pe and Da, the (R_b, R_c) phase plane can be divided into four zones as described below and shown in figure 12. The flow is stable below the solid curve and is denoted as Zone IV. While above the solid curve, the flow becomes unstable and can be divided into three parts as follows. Here, above the dashed lines (Zone I) is the zone where flow remains unstable with or without reaction. Further, the region confined between solid curve and dashed lines (Zones II and III) is also an unstable region. In Zone II, reactions induce instability by decreasing the viscosity, whereas in Zone III, instability is induced by reaction that increases viscosity.

REFERENCES

BABAEI, M. & ISLAM, A. 2018 Convective-reactive CO_2 dissolution in aquifers with mass transfer with immobile water. *Water Resour. Res.* **54** (11), 9585–9604.

BEN, Y., DEMEKHIN, E.A. & CHANG, H.-C. 2002 A spectral theory for small-amplitude miscible fingering. *Phys. Fluids* **14** (3), 999–1010.

BISCHOFBERGER, I., RAMACHANDRAN, R. & NAGEL, S.R. 2014 Fingering versus stability in the limit of zero interfacial tension. *Nat. Commun.* **5** (1), 1–6.

BRAU, F., SCHUSZTER, G. & DE WIT, A. 2017 Flow control of $A + B \rightarrow C$ fronts by radial injection. *Phys. Rev. Lett.* **118** (13), 134101.

CATCHPOOLE, H.J., SHALLIKER, R.A., DENNIS, G.R. & GUIOCHON, G. 2006 Visualising the onset of viscous fingering in chromatography columns. *J. Chromatogr.* A **1117** (2), 137–145.

CHEN, C.Y., HUANG, C.W., GADÊLHA, H. & MIRANDA, J.A. 2008 Radial viscous fingering in miscible hele-shaw flows: a numerical study. *Phys. Rev.* E **78** (1), 016306.

CHEN, J.-D. 1987 Radial viscous fingering patterns in Hele-Shaw cells. *Exp. Fluids* **5** (6), 363–371.

CHEN, Y.-F., FANG, S., WU, D.-S. & HU, R. 2017 Visualizing and quantifying the crossover from capillary fingering to viscous fingering in a rough fracture. *Water Resour. Res.* **53** (9), 7756–7772.

CHUI, J.Y.Y., DE ANNA, P. & JUANES, R. 2015 Interface evolution during radial miscible viscous fingering. *Phys. Rev.* E **92** (4), 041003.

CORREDOR, L., MAINI, B. & HUSEIN, M. 2018 Improving polymer flooding by addition of surface modified nanoparticles. In *SPE Asia Pacific Oil and Gas Conference and Exhibition*. OnePetro.

CUBAUD, T. & MASON, T.G. 2012 Interacting viscous instabilities in microfluidic systems. *Soft Matt.* **8** (41), 10573–10582.

DANIEL, D., TILTON, N. & RIAZ, A. 2013 Optimal perturbations of gravitationally unstable, transient boundary layers in porous media. *J. Fluid Mech.* **727**, 456–487.

DE WIT, A. 2020 Chemo-hydrodynamic patterns and instabilities. *Annu. Rev. Fluid Mech.* **52**, 531–555.

DE WIT, A. & HOMSY, G.M. 1999 Viscous fingering in reaction-diffusion systems. *J. Chem. Phys.* **110** (17), 8663–8675.

DELANNOY, E., TELLIER, G., CHOLET, J., LEROY, A.M., TREIZEBRÉ, A. & SONCIN, F. 2022 Multi-layered human blood vessels-on-chip design using double viscous finger patterning. *Biomedicines* **10** (4), 797.

DENTZ, M., LE BORGNE, T., ENGLERT, A. & BIJELJIC, B. 2011 Mixing, spreading and reaction in heterogeneous media: a brief review. *J. Contam. Hydrol.* **120–121**, 1–17.

DONG, R., WHEELER, M.F., MA, K. & SU, H. 2020 A 3D acid transport model for acid fracturing treatments with viscous fingering. In *SPE Annual Technical Conference and Exhibition*. OnePetro.

FAKHARI, A., LI, Y., BOLSTER, D. & CHRISTENSEN, K.T. 2018 A phase-field lattice Boltzmann model for simulating multiphase flows in porous media: application and comparison to experiments of CO_2 sequestration at pore scale. *Adv. Water Resour.* **114**, 119–134.

FANI, M., POURAFSHARY, P., MOSTAGHIMI, P. & MOSAVAT, N. 2022 Application of microfluidics in chemical enhanced oil recovery: a review. *Fuel* **315**, 123225.

GÉRARD, T. & DE WIT, A. 2009 Miscible viscous fingering induced by a simple $A + B \rightarrow C$ chemical reaction. *Phys. Rev.* E **79** (1), 016308.

GREEN, D.W., WILLHITE, G.P., *et al.* 1998 *Enhanced Oil Recovery*, vol. 6. Henry L. Doherty Memorial Fund of AIME, Society of Petroleum Engineers.

HEJAZI, S.H., TREVELYAN, P.M.J., AZAIEZ, J. & DE WIT, A. 2010 Viscous fingering of a miscible reactive $A + B \rightarrow C$ interface: a linear stability analysis. *J. Fluid Mech.* **652**, 501–528.

HOTA, T.K. & MISHRA, M. 2018 Non-modal stability analysis of miscible viscous fingering with non-monotonic viscosity profiles. *J. Fluid Mech.* **856**, 552–579.

HOTA, T.K., PRAMANIK, S. & MISHRA, M. 2015a Nonmodal linear stability analysis of miscible viscous fingering in porous media. *Phys. Rev.* E **92** (5), 053007.

HOTA, T.K., PRAMANIK, S. & MISHRA, M. 2015b Onset of fingering instability in a finite slice of adsorbed solute. *Phys. Rev.* E **92** (2), 023013.

HUPPERT, H.E. & NEUFELD, J.A. 2014 The fluid mechanics of carbon dioxide sequestration. *Annu. Rev. Fluid Mech.* **46**, 255–272.

JIANG, J., JAMES, S.C. & MOJARAB, M. 2020 A multiphase, multicomponent reservoir-simulation framework for miscible gas and steam coinjection. *SPE Res. Eval. Engng* **23** (02), 551–565.

JIMÉNEZ-MARTÍNEZ, J., PORTER, M.L., HYMAN, J.D., CAREY, J.W. & VISWANATHAN, H.S. 2016 Mixing in a three-phase system: enhanced production of oil-wet reservoirs by CO_2 injection. *Geophys. Res. Lett.* **43** (1), 196–205.

KIM, M.C., PRAMANIK, S., SHARMA, V. & MISHRA, M. 2021 Unstable miscible displacements in radial flow with chemical reactions. *J. Fluid Mech.* **917**, A25.

LEI, T. & LUO, K.H. 2021 Pore-scale simulation of miscible viscous fingering with dissolution reaction in porous media. *Phys. Fluids* **33** (3), 034134.

LIU, F., LU, P., ZHU, C. & XIAO, Y. 2011 Coupled reactive flow and transport modeling of CO_2 sequestration in the Mt. Simon sandstone formation, Midwest USA. *Intl J. Greenh. Gas Control* **5** (2), 294–307.

MAHARDIKA, M.A., SHE, Y., SHORI, F., PATMONOAJI, A., MATSUSHITA, S., SUEKANE, T. & NAGATSU, Y. 2021 Enhanced heavy oil recovery by calcium hydroxide flooding with the production

of viscoelastic materials: study with 3-D x-ray tomography and 2-D glass micromodels. *Energy Fuels* **35** (14), 11210–11222.

MAINSTER, M.A. 1990 The fractal properties of retinal vessels: embryological and clinical implications. *Eye* **4** (1), 235–241.

MATAR, O.K. & TROIAN, S.M. 1999 Spreading of a surfactant monolayer on a thin liquid film: onset and evolution of digitated structures. *Chaos* **9** (1), 141–153.

MATSUSHITA, M. & FUJIKAWA, H. 1990 Diffusion-limited growth in bacterial colony formation. *Physica* A **168** (1), 498–506.

MAYER, E.H., BERG, R.L., CARMICHAEL, J.D. & WEINBRANDT, R.M. 1983 Alkaline injection for enhanced oil recovery-a status report. *J. Petrol. Technol.* **35** (01), 209–221.

MICHIOKA, T. & KOMORI, S. 2004 Large-eddy simulation of a turbulent reacting liquid flow. *AIChE* **50** (11), 2705–2720.

MISHRA, M., MARTIN, M. & DE WIT, A. 2008 Differences in miscible viscous fingering of finite width slices with positive or negative log-mobility ratio. *Phys. Rev.* E **78** (6), 066306.

MUGGERIDGE, A., COCKIN, A., WEBB, K., FRAMPTON, H., COLLINS, I., MOULDS, T. & SALINO, P. 2014 Recovery rates, enhanced oil recovery and technological limits. *Phil. Trans. R. Soc.* A **372** (2006), 20120320.

NAGATSU, Y. & DE WIT, A. 2011 Viscous fingering of a miscible reactive $A + B \rightarrow C$ interface for an infinitely fast chemical reaction: nonlinear simulations. *Phys. Fluids* **23** (4), 043103.

NAGATSU, Y., KONDO, Y., KATO, Y. & TADA, Y. 2009 Effects of moderate Damköhler number on miscible viscous fingering involving viscosity decrease due to a chemical reaction. *J. Fluid Mech.* **625**, 97–104.

NAGATSU, Y., MATSUDA, K., KATO, Y. & TADA, Y. 2007 Experimental study on miscible viscous fingering involving viscosity changes induced by variations in chemical species concentrations due to chemical reactions. *J. Fluid Mech.* **571**, 475–493.

NAGATSU, Y. & UEDA, T. 2001 Effects of reactant concentrations on reactive miscible viscous fingering. *AIChE* **47** (8), 1711–1720.

NAGATSU, Y. & UEDA, T. 2003 Effects of finger-growth velocity on reactive miscible viscous fingering. *AIChE J.* **49** (3), 789–792.

PATERSON, L. 1985 Fingering with miscible fluids in a Hele-Shaw cell. *Phys. Fluids* **28** (1), 26–30.

PEI, H., ZHANG, G., GE, J., TANG, M. & ZHENG, Y. 2012 Comparative effectiveness of alkaline flooding and alkaline–surfactant flooding for improved heavy-oil recovery. *Energy Fuels* **26** (5), 2911–2919.

POJMAN, J.A. 2010 *Frontal Polymerization*. Wiley-VCH Verlag GmbH & Co. KGaA.

PRAMANIK, S., HOTA, T.K. & MISHRA, M. 2015 Influence of viscosity contrast on buoyantly unstable miscible fluids in porous media. *J. Fluid Mech.* **780**, 388–406.

RANA, C., PRAMANIK, S., MARTIN, M., DE WIT, A. & MISHRA, M. 2019 Influence of langmuir adsorption and viscous fingering on transport of finite size samples in porous media. *Phys. Rev. Fluids* **4** (10), 104001.

RICHARDSON, J.P. & NICKLOW, J.W. 2002 In situ permeable reactive barriers for groundwater contamination. *Soil Sediment Contam.* **11** (2), 241–268.

RIOLFO, L.A., NAGATSU, Y., IWATA, S., MAES, R., TREVELYAN, P.M.J. & DE WIT, A. 2012 Experimental evidence of reaction-driven miscible viscous fingering. *Phys. Rev.* E **85** (1), 015304.

SAINZ-GARCIA, A., ABARCA, E., NARDI, A., GRANDIA, F. & OELKERS, E.H. 2017 Convective mixing fingers and chemistry interaction in carbon storage. *Intl J. Greenh. Gas Control* **58**, 52–61.

SCHMID, P.J. 2007 Nonmodal stability theory. *Annu. Rev. Fluid Mech.* **39** (1), 129–162.

SEDAGHAT, M., MOHAMMADZADEH, O., KORD, S. & CHATZIS, I. 2016 Heavy oil recovery using asp flooding: a pore-level experimental study in fractured five-spot micromodels. *Can. J. Chem. Engng* **94** (4), 779–791.

SHALLIKER, R.A., CATCHPOOLE, H.J., DENNIS, G.R. & GUIOCHON, G. 2007 Visualising viscous fingering in chromatography columns: high viscosity solute plug. *J. Chromatogr.* A **1142** (1), 48–55.

SHARMA, V., CHEN, C.-Y. & MISHRA, M. 2023 A linear stability analysis of instabilities with reactive flows in porous medium. *Phys. Fluids* **35** (6), 064105.

SHARMA, V., NAND, S., PRAMANIK, S., CHEN, C.-Y. & MISHRA, M. 2020 Control of radial miscible viscous fingering. *J. Fluid Mech.* **884**, A16.

SHARMA, V., PRAMANIK, S., CHEN, C.-Y. & MISHRA, M. 2019 A numerical study on reaction-induced radial fingering instability. *J. Fluid Mech.* **862**, 624–638.

SHEN, S.F. 1961 Some considerations on the laminar stability of time-dependent basic flows. *Aerosp. Sci. J.* **28** (5), 397–404.

STREITBERGER, K.-J., LILAJ, L., SCHRANK, F., BRAUN, J., HOFFMANN, K.-T., REISS-ZIMMERMANN, M., KÄS, J.A. & SACK, I. 2020 How tissue fluidity influences brain tumor progression. *Proc. Natl Acad. Sci.* **117** (1), 128–134.

SUN, Z., WU, X., KANG, X., LU, X., LI, Q., JIANG, W. & ZHANG, J. 2019 Comparison of oil displacement mechanisms and performances between continuous and dispersed phase flooding agents. *Pet. Explor. Dev.* **46** (1), 121–129.

TAN, C.T. & HOMSY, G.M. 1986 Stability of miscible displacements in porous media: rectilinear flow. *Phys. Fluids* **29** (11), 3549–3556.

TAN, C.T. & HOMSY, G.M. 1987 Stability of miscible displacements in porous media: radial source flow. *Phys. Fluids* **30** (5), 1239–1245.

TILTON, N., DANIEL, D. & RIAZ, A. 2013 The initial transient period of gravitationally unstable diffusive boundary layers developing in porous media. *Phys. Fluids* **25** (9), 092107.

TREFETHEN, L.N., TREFETHEN, A.E., REDDY, S.C. & DRISCOLL, T.A. 1993 Hydrodynamic stability without eigenvalues. *Science* **261** (5121), 578–584.

VERMA, P., SHARMA, V. & MISHRA, M. 2022 Radial viscous fingering induced by an infinitely fast chemical reaction. *J. Fluid Mech.* **945**, A19.

VERMA, P., SHARMA, V. & MISHRA, M. 2023 Understanding stable/unstable miscible $A + B \rightarrow C$ reaction front and mixing in porous medium. *Phys. Fluids* **35**, 044102.

VIDEBÆK, T.E. & NAGEL, S.R. 2019 Diffusion-driven transition between two regimes of viscous fingering. *Phys. Rev. Fluids* **4** (3), 033902.

WANG, W., ZHANG, C., PATMONOAJI, A., HU, Y., MATSUSHITA, S., SUEKANE, T. & NAGATSU, Y. 2021 Effect of gas generation by chemical reaction on viscous fingering in a Hele-Shaw cell. *Phys. Fluids* **33** (9), 093104.

WEIDONG, L., LITAO, L., GUANGZHI, L., LUO, Z., YUNYUN, W. & JIANG, W. 2017 Experimental study on the mechanism of enhancing oil recovery by polymer–surfactant binary flooding. *Pet. Explor. Dev.* **44** (4), 636–643.